ADVANCED FUNCTIONAL MATERIALS
www.afm-journal.de

Mitigating Ring-Opening to Develop Stable TEMPO Catholytes for pH-Neutral All-organic Redox Flow Batteries

Hao Fan, Wenda Wu, Mahalingam Ravivarma, Hongbin Li, Bo Hu, Jiafeng Lei, Yangyang Feng, Xiaohua Sun, Jiangxuan Song, and Tianbiao Leo Liu**

Redox-active organics are highly attractive in aqueous organic redox flow batteries (AORFBs). However, the lack of capacity dense, stable organic catholytes remains a challenge to develop energy-dense, long cycle-life AORFBs. Herein, a stable organic catholyte, 4-[3-(trimethylammonium) acetylamino]-2,2,6,6-tetramethylpiperidine-1-oxyl chloride (TMAAcNHTEMPO) is developed through rational molecular engineering using connective acetamido and trimethylammonium groups. Paired with bis-(trimethylammonium) propyl viologen tetrachloride anolyte, stable AORFBs (up to 1500 cycles) with a low capacity fade rate of ca. 0.0144% h^{-1} are achieved. Experimental characterizations and theoretical simulations revealed that TMAAcNH-TEMPO is largely stabilized by the reduced reactivity of the nitroxyl radical moiety that mitigates a ring-opening side reaction.

1. Introduction

Renewable sources such as solar and wind play a key role in building a sustainable and green energy powered society.[1,2] Nonetheless, the widespread adoption and growing penetrations of those sources are significantly impeded by the inherent intermittency and consequent impacts when supplied to power grids.[1,2] Aqueous organic redox flow batteries (AORFBs) are regarded as an effective electrochemical energy storage technology that could address the limitation of intermittent energy sources owing to the resource-abundant elements, flexible structure tunability, eco-/bio-friendliness, and multi-electron transfer characteristics of redox-active organics.[2–5] The rapid progress of advanced redox-active organic electrolytes has been achieved in AORFBs technologies over the past ten years in three main classes: i) pH-neutral viologen,[6–10] ferrocene,[11,12] nitroxide radical,[6,13–15] and near pH-neutral quinone-based AORFBs,[16] ii) alkaline quinone,[17,18] phenzine[19,20] and ketone[21,22] AORFBs, and iii) acidic benzo/anthraquinone[23–25] and phenothiazine[26] based AORFBs. Highly acidic and/or highly alkalic AORFBs are operating in strong caustic conditions and are prone to fast capacity decay because acidic or alkaline solutions are highly detrimental to the stability of redox-active materials and other cell components such as membranes and electrodes. In stark contrast, moderate pH-neutral AORFBs have demonstrated superior capacity retention because of the much improved chemical stability of redox-active molecules at pH neutral conditions.[2] The last several years have witnessed the rapid progress of pH neutral AORFBs.[2] For example, sulfonate viologen based AORFBs have achieved cycling stability up to 1000 cycles (30 days) at an energy density of 9.6 Wh L^{-1}.[9] Thereby, it is realistic to expand pH-neutral AORFBs to meet the performance and cost target (<\$150 kWh^{-1}) of redox flow batteries for large-scale energy storage recommended by the United States Department of Energy.[27]

However, the cycling stability and energy densities of pH neutral AORFBs are primarily limited by the lack of comparable catholytes molecules.[2,28] 2,2,6,6-tetramethylpiperidine 1-oxyl (TEMPO) species have been recognized as promising catholyte candidates for pH-neutral AORFBs.[2] Since the first report of 2,2,6,6-tetramethylpiperidine 1-oxyl (4-OH-TEMPO),[6] a few TEMPO molecules have been developed with improved battery performance in recent years.[13–15] Despite the advancements achieved in TEMPO-based catholytes, most of them still experience a high temporal capacity fade rate of >1%/day and further limit their application potential. Such short lifetimes cannot meet the expected >10 years of service life for widespread market penetration. Thus, ultra-stable and low-cost cathodic TEMPO derivatives are highly desired for long-life AORFBs. In addition, in-depth mechanistic understandings of the chemical stability of TEMPO catholytes are scarce but are critical to designing persistent TEMPO catholytes.

Herein, we report a stable nitroxyl radical catholyte 4-[3-(trimethylammonium)acetylamino]-2,2,6,6-tetramethylpiperidine-1-oxyl chloride (TMAAcNH-TEMPO) by molecular engineering strategy of grafting the acetylamino and trimethylammonium

H. Fan, M. Ravivarma, H. Li, B. Hu, J. Lei, Y. Feng, J. Song
State Key Laboratory for Mechanical Behavior of Materials
Shaanxi International Research Center for Soft Matter
Xi'an Jiaotong University
Xi'an 710049, China
E-mail: songjx@xjtu.edu.cn
W. Wu, T. L. Liu
Department of Chemistry and Biochemistry
Utah State University
Logan, UT 84322, USA
E-mail: leo.liu@usu.edu
X. Sun
College of Materials and Chemical Engineering
China Three Gorges University
Yichang 443002, China
The ORCID identification number(s) for the author(s) of this article can be found under https://doi.org/10.1002/adfm.202203032.

DOI: 10.1002/adfm.202203032

groups onto TEMPO. When paired with 1,1′-bis[3-(trimethylammonium)propyl]-4,4′-bipyridinium tetrachloride ($(NPr)_2V$) anolyte, the TMAAcNH-TEMPO/$(NPr)_2V$ AORFB exhibits a fairly low capacity fade rate of < 0.346% per day over 40 days under consecutive galvanostatic cycling, which is among the best stability reported in the TEMPO-based AORFBs to the best of our knowledge. In addition, the high solubility of TMAAcNH-TEMPO (4.30 M) makes it promising for developing high-energy-density AORFBs. We further reveal the ring-opening degradation mechanism of the oxoammonium state of TEMPO, which could be suppressed by amidation together with cationic groups.

2. Results and Discussion

The TMAAcNH-TEMPO catholyte was synthesized via an amidation strategy in two successive steps, as shown in **Figure 1**a. Briefly, monochloroacetic acid reacted with 4-NH_2-TEMPO to form an acyl chloride intermediate. Afterward, acyl chloride intermediate reacted with trimethylamine to produce the final product TMAAcNH-TEMPO in a good yield (84.6%). The assortative $(NPr)_2V$ anolyte was prepared by a modified route.[29] The structures of TMAAcNH-TEMPO and $(NPr)_2V$ were characterized by nuclear magnetic resonance (NMR) spectroscopy (Figures S1–S3, Supporting Information).

The cyclic voltammetry (CV) study of TMAAcNH-TEMPO at a scan rate of 100 mV s^{-1} gives a reversible redox potential ($E_{1/2}$) at 0.84 V (vs NHE) in 1.0 M KCl, close to that of the precursor, 4-NH_2-TEMPO (0.90 V, Figure 1b). Under different scan rates, the oxidation and reduction peaks of $E_{1/2}$ keep constant with the increasing scan rate (Figure S4a, Supporting Information). According to the Nicholson method,[2,30] the observed peak separations (ΔE) of 63–66 mV leads to an electron transfer rate constant k^0 of >0.35 (Figure S4c,d, Supporting Information), implying good reversibility of the redox couple. In addition, the corresponding peak currents I_{pa} and I_{pc} in the redox process of TMAAcNH-TEMPO show a linear relationship with the square root of scan rate $v^{1/2}$ (Figure S4b, Supporting Information), which indicates the interconversion of the TMAAcNH-TEMPO/TMAAcNH-TEMPO$^+$ redox couple is a diffusion-controlled process in the stagnant electrolyte.

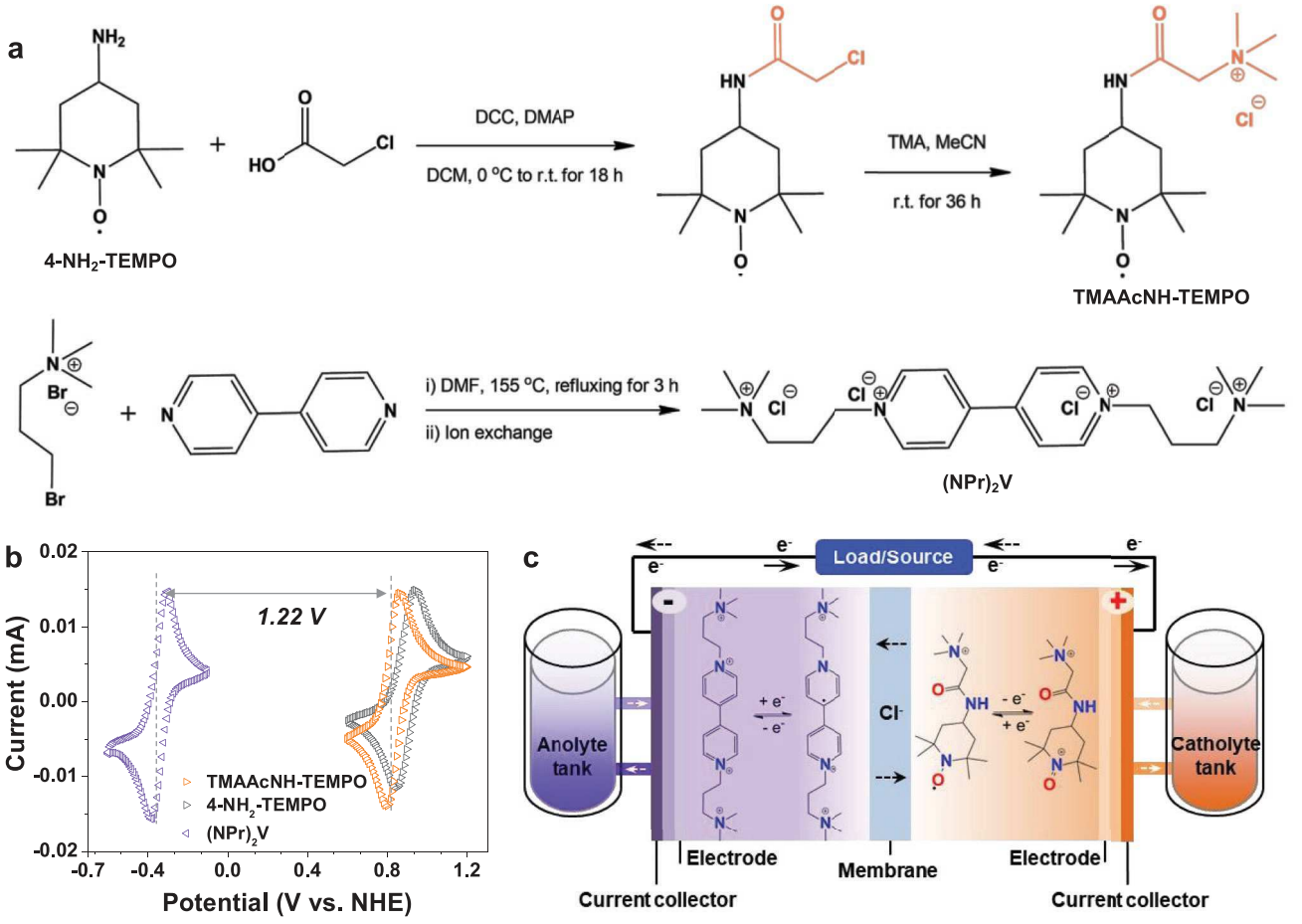

Figure 1. Synthesis of TMAAcNH-TEMPO and $(NPr)_2V$ and their applications as redox-active electrolytes in pH-neutral AORFBs. a) Synthetic routes for TMAAcNH-TEMPO and $(NPr)_2V$. b) CV curves of 2.0×10^{-3} M TMAAcNH-TEMPO (yellow trace), 4-NH_2-TEMPO (gray trace), and $(NPr)_2V$ (purple trace). The electroactive compounds were tested in a 1.0 M KCl solution at a scan rate of 100 mV s^{-1} on a glassy carbon electrode. c) Schematic of a pH-neutral AORFB assembled with TMAAcNH-TEMPO catholyte and $(NPr)_2V$ anolyte with Cl^- as a charge carrier passing through an anion exchange membrane.

Table 1. Electrochemical and physicochemical properties of TMAAcNH-TEMPO, 4-NH_2-TEMPO, and $(NPr)_2V$.

Electrolyte	$E_{1/2}$ [V vs NHE]	$D_0 \times 10^{-5}$ [cm^2 s^{-1}]	k^0 [cm s^{-1}]	Solubility [M, in water]	Refs.
TMAAcNH-TEMPO	0.84	0.55	0.422	≈4.3	This study
4-NH_2-TEMPO	0.90	0.38	–	>5.0	[31,32]
$(NPr)_2V$	–0.38	0.39	0.309	>2.0	[12,29]

Linear sweep voltammogram of TMAAcNH-TEMPO collected with a rotating disk electrode displays the mass-transport controlled limiting current in well-defined plateau shapes at all rotation rates (Figure S5, Supporting Information). The corresponding limiting current showed a linear relationship with the square root of rotating angular velocity, which indicates the redox process of TMAAcNH-TEMPO is a diffusion-controlled process. According to the Levich plot and equation, the diffusion coefficient (D_0) of TMAAcNH-TEMPO was determined to be 5.52×10^{-6} cm^2 s^{-1}. The D_0 and k^0 of these compounds (**Table 1**) are 2–8 times higher than those of redox-active organic quinonoid compounds,[16,33–35] and organometallic species[19,36] as well as magnitude of orders higher than those for inorganic vanadium ions.[37,38]

Accordingly, we assembled a pH-neutral AORFB with a full cell voltage of 1.22 V using the combination of TMAAcNH-TEMPO catholyte and $(NPr)_2V$ anolyte separated by a piece of HUAMOTECH AEM (Figure 1c). Equations in Figure 1c give the cathodic and anodic half-cell reactions for the pH-neutral TMAAcNH-TEMPO/$(NPr)_2V$ AORFB. For the charging process, the TMAAcNH-TEMPO is oxidized to the oxoammonium as the charge state. Correspondingly, the $[(NPr)_2V]^{4+}$ in the anolyte is first reduced to the cation radical $[(NPr)_2V]^{3+}$ at –0.38 V. TMAAcNH-TEMPO is the capacity-limiting side in the AORFB. For comparison, a 4-NH_2-TEMPO/$(NPr)_2V$ AORFB was also constructed and operated under the same conditions.

TMAAcNH-TEMPO/$(NPr)_2V$ AORFB were first explored using 0.1 M catholyte and anolyte with a volume ratio of 7:10 in a 1.0 M KCl supporting electrolyte (**Figure 2**). The rate performance was examined from 10 to 50 mA cm^{-2} with an increment of 10 mA cm^{-2} and a cut-off window of 0.7 and 1.5 V (Figures 2a; Figure S6, Supporting Information). The increase of the cycling rate leads to decreased capacity outputs from 2.63 Ah L^{-1} at 10 mA cm^{-2} (97.9% capacity utilization) to 2.48 Ah L^{-1} at 50 mA cm^{-2} (92.7% capacity utilization). The gradually decreasing rate capacity is attributed to the increased ohmic loss as indicated by the voltage gaps of the charge and discharge voltage profiles at different rates (Figure 2b). Correspondingly, the energy efficiency (EE) drops with the increased rates from 93% at 10 mA cm^{-2} to 79% at 50 mA $cm^{-2,}$ while a consistent CE of over 99.9% is observed at these rates (Figure 2b).

Prolonged galvanostatic cycling was performed at 50 mA cm^{-2} to probe the lifetime of the AORFBs (Figure 2c). The discharge capacity (2.48 Ah L^{-1}) can achieve a high capacity utilization of 92.6%. The TMAAcNH-TEMPO/$(NPr)_2V$ AORFB exhibits a significantly long lifetime of 1500 cycles or 347 h with Coulombic efficiency (CE) of >99.9% and energy efficiency (EE) of 78% (Figures 2c; Figure S7, Supporting Information). The TMAAcNH-TEMPO/$(NPr)_2V$ AORFB retains 95% of the initial capacity after 1500 cycles, projecting an apparent capacity fade rate of 0.0033%/cycle or a temporal capacity loss rate of 0.0144% h^{-1} (Figure 2c,d). In contrast, the reference battery of 4-NH_2-TEMPO lost 59% of its original capacity over 600 cycles (Figure 2c,e). The temporal capacity loss rate of the reference battery, 0.5860% h^{-1}, is almost 41 times higher than that of the TMAAcNH-TEMPO/$(NPr)_2V$ AORFB. It should be noticed that the pH of TMAAcNH-TEMPO catholyte changes from the initial 6.91 to 5.92 by the end of cycling, which is more stable than that of 4-NH_2-TEMPO, from 7.61 to 2.63 (Figure S8, Supporting Information). The reduced acidification indicates that side reactions such as ring-opening and disproportionation are greatly suppressed for TMAAcNH-TEMPO, which is discussed below.

The crossover and stability of electroactive species are two major factors for the cycling lifetime of an AORFB. The capacity loss due to the crossover of 0.1 M TMAAcNH-TEMPO- and 4-NH_2-TEMPO-based AORFBs toward the AEM was examined by using the dynamic ohmic-compensated CV method (Figure S9, Supporting Information). The ohmic-compensated CV measurements for TMAAcNH-TEMPO catholyte present a small current decrease (≈4.3%), while CV curves for 4-NH_2-TEMPO catholyte show a ≈60.3% current loss (Figure S9a,c, Supporting Information) after the consecutive charge-discharge cycles. Besides, CV traces of the corresponding anolytes show similar redox behaviors to the catholytes, suggesting the migrations of nitroxyl radicals from the catholyte to the anolyte (Figure S9b,d, Supporting Information). Based on the measurements, it is interesting TMAAcNH-TEMPO and 4-NH_2-TEMPO showed comparable crossover possibility. We also calculated that the crossover contributed to 84.5% of capacity lost in the TMAAcNH-TEMPO-based AORFB, and only 11.1% of the capacity lost in the reference 4-NH_2-TEMPO-based one because the capacity loss of 4-NH_2-TEMPO is mostly caused by the chemical degradation (Figure 2c; Figure S10, Supporting Information). Furthermore, an unbalanced compositionally symmetric battery cycling method was performed to investigate the source of capacity loss and eliminate the effect of crossover. Over 140 h (200 cycles), the TMAAcNH-TEMPO symmetric battery lost roughly 2.3% of its initial capacity, equating to roughly 0.0158% h^{-1} (Figure S11, Supporting Information), which is in reasonable agreement with the fade rate observed in the full-battery study (0.0144% h^{-1}). These results indicate that TMAAcNH-TEMPO is structurally more stable than 4-NH_2-TEMPO.

The electron paramagnetic resonance (EPR), UV–Vis, NMR, and electrospray ionization mass spectra (ESI-MS) measurements were performed to understand the stabilization/failure mechanism. Several samples were taken from the cycled 0.1 M TMAAcNH-TEMPO and 4-NH_2-TEMPO based AORFBs for the above-mentioned analyzes, respectively (**Figure 3**; Figures S12–S16, Supporting Information). The nitroxyl radical concentrations estimated from the EPR spectra present a linear relationship with the remaining capacity (Figure 3a; Figure S12, Supporting Information), quantitatively consistent with the as-discussed CV characterizations. The slopes of the fitted lines suggest that the number of redox-active molecules involved in the charge–discharge process (Δn) is generally equal to the number of consumed electrons (e) (Figure S12, Supporting Information).

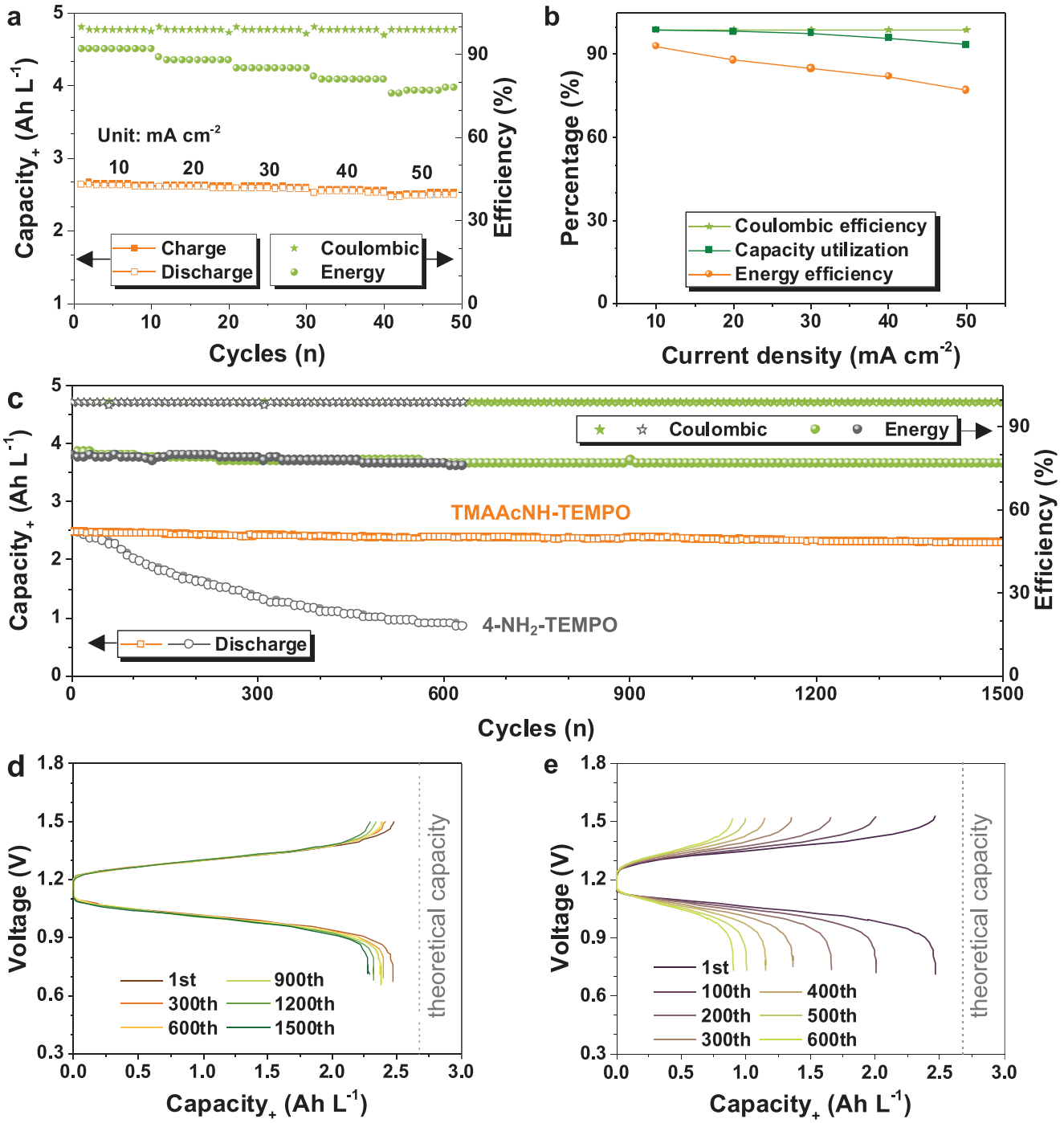

Figure 2. Energy Storage Performance of pH-neutral AORFBs assembled with TMAAcNH-TEMPO or 4-NH_2-TEMPO (0.1 M) as a catholyte (7.0 mL) and $(NPr)_2V$ (0.1 M) as an anolyte (10.0 mL). a) Charge–discharge capacity, CE, and EE of the TMAAcNH-TEMPO/$(NPr)_2V$ AORFB at the current densities of 10, 20, 30, 40, and 50 mA cm^{-2}. b) The corresponding plots of CE, EE, and capacity utilization versus the current density of the battery. c) Galvanostatic cycling of TMAAcNH-TEMPO/$(NPr)_2V$ AORFB (orange) and the reference 4-NH_2-TEMPO/$(NPr)_2V$ (black) at 50 mA cm^{-2} for 1500 and 600 consecutive cycles, respectively. Charge–discharge capacity, CE, and EE were plotted versus the cycle number. d,e) Representative charge–discharge curves of d) TMAAcNH-TEMPO/$(NPr)_2V$ and e) 4-NH_2-TEMPO/$(NPr)_2V$.

Time-dependent UV–Vis spectra of the TMAAcNH-TEMPO and 4-NH_2-TEMPO catholytes present negligible absorption changes for the former but significant reductions for the latter in both discharged and charged states (Figure 3b,c). It was observed that both the discharged and charged states of 4-NH_2-TEMPO experienced apparent absorption decay. The improved radical stability of TMAAcNH-TEMPO over 4-NH_2-TEMPO is likely attributed to the reduced radical–radical bimolecular degradations. It is noted that the charged state of 4-NH_2-TEMPO underwent even more rapid degradation than the discharged state (Figure 3b,c,

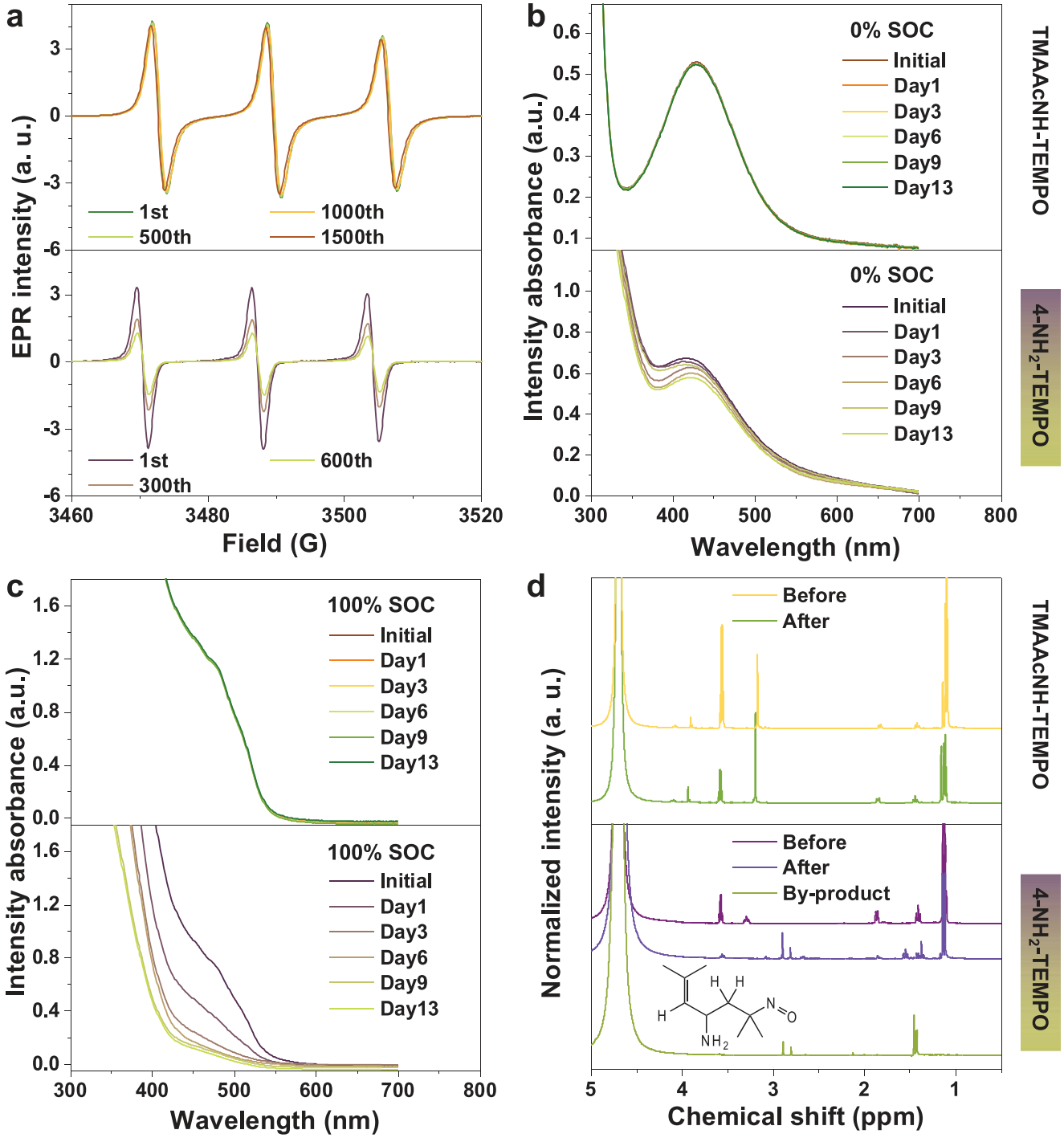

Figure 3. Stabilization mechanism of the pH-neutral TMAAcNH-TEMPO-based AORFB. a) EPR spectra of the TMAAcNH-TEMPO (top) and 4-NH_2-TEMPO (bottom) catholyte after the different cycles. b,c) Time-dependent UV–Vis spectra of TMAAcNH-TEMPO and 4-NH_2-TEMPO catholytes with two SOCs of b) 0% and c) 100% , respectively. d) Partial enlargement of ^{1}H NMR spectra in D_2O (Full ^{1}H NMR spectra are displayed in Figures S13 and S14, Supporting Information) for the two catholytes before and after consecutive charge-discharge cycling.

bottom), The result suggests the charge state, 4-NH_2-TEMPO$^+$ is mainly responsible for the capacity decay.

No obvious change was observed in the ^{1}H NMR spectra of TMAAcNH-TEMPO after 1500 cycles of battery operation (Figure 3d), while a new set of proton signals appeared in the ^{1}H NMR spectra of 4-NH_2-TEMPO after 600 cycles (Figure 3d; Figure S13, Supporting Information). The by-product was isolated and characterized as a ring-opening product of the 4-NH_2-TEMPO by NMR and ESI-MS analyses (Figure 3d; Figures S14–S16, Supporting Information). The ring-opening product was assigned as 2,6-dimethyl-2-nitrosohept-5-en-4-amine. According to the NMR and UV–Vis results, it is proposed that

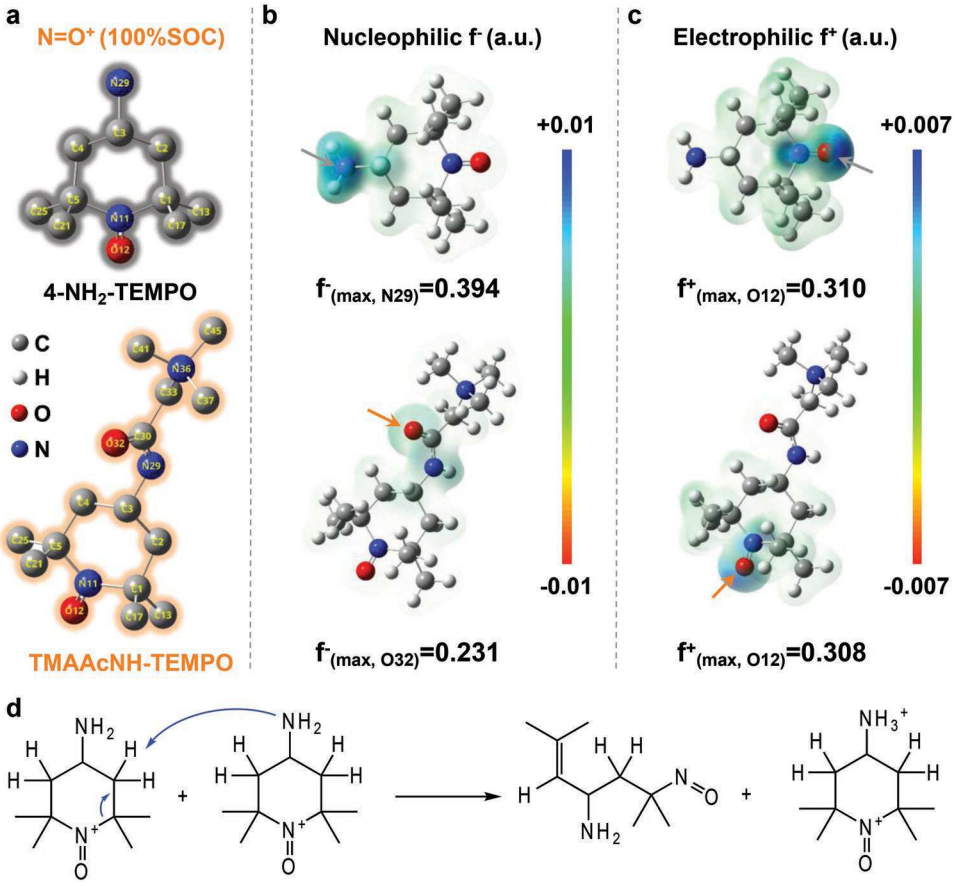

Figure 4. DFT simulations of 4-NH_2-TEMPO$^+$ and TMAAcNH-TEMPO$^+$ with 100%SOC. a) Labels and symbols of molecular skeleton atoms. b) Nucleophilic Fukui function f^- isosurfaces and the maximal f^- values. c) Electrophilic Fukui function f^+ isosurfaces and the maximal f^+ values. d) Proposed ring-opening side reaction scheme.

the built-in -NH_2 base of 4-NH_2-TEMPO promotes the deprotonation of the oxoammonium charged state to yield the ring-opening by-product.[2] The scheme in **Figure 4**d below illustrated the ring-opening degradation mechanism of the oxoammonium charged state of 4-NH_2-TEMPO. ESI-MS spectra for the initial TMAAcNH-TEMPO and 4-NH_2-TEMPO find only one major protonated product [(M+2)$^+$] with the respective mass-to-charge ratio of 308.85 and 173.15 in the positive ionization mode (Figure S17, Supporting Information). For the cycled TMAAcNH-TEMPO, the mass-to-charge ratio is still located at 308.85 with the proximal level (Figure S17, Supporting Information). However, for the 4-NH_2-TEMPO catholyte, another primary product [(M-31)$^+$] was detected with the mass-to-charge ratio of 140.15 (Figure S17, Supporting Information), which is assigned as the N=O removal product (2,6-dimethyl-2,5-dien-4-heptylamine) of the ring-opening by-product in the ring-opening scheme. It is believed that the pH change from 7.61 to 2.63 of the the 4-NH_2-TEMPO catholyte during cycling is associated with the ring-opening degradation. These post-cycling analysis results demonstrate the much more suppressed ring-opening side reaction for TMAAcNH-TEMPO than 4-NH_2-TEMPO. Therefore, the improved stability of TMAAcNH-TEMPO benefits the retention of the battery capacity.

Furthermore, density functional theory (DFT) simulation was conducted to provide a mechanism insight on the better stability of TMAAcNH-TEMPO than 4-NH_2-TEMPO in the oxoammonium form with 100%SOC (Figure 4; Figures S18–S20, Supporting Information). Condensed Fukui function (*f*), defined as the amount of electron density distribution around atoms, is a useful method to predict electrophilic/nucleophilic reactive sites.[26,29,39,40] As shown in Figure 4a,c, both nucleophilic f^- and electrophilic f^+ isosurfaces for $^+$N=O forms are in the same color distribution order of TMAAcNH-TEMPO < 4-NH_2-TEMPO. The TMAAcNH-TEMPO shows the maximal f^- and f^+ values of 0.231 and 0.308 for respective O32 and O12 skeleton atoms, which are lower than 0.394 and 0.310 for N29 and O12 in 4-NH_2-TEMPO skelecton (Figure 4b,c; Tables S1 and S2, Supporting Information). Especially, the decreased *f* values and transferred reactive site represent the less likely to electrophilic/nucleophilic attack for TMAAcNH-TEMPO, resulting the improved chemical stability.[40,41] Noticeably, the maximal nucleophilic f^- region of 4-NH_2-TEMPO$^+$ is centered on the NH_2-C segment meanwhile the electrophilic f^+ region is along with the $^+$N=O moiety. Accordingly, we can illustrate the ring-opening degradation mechanism of the oxoammonium charged state of 4-NH_2-TEMPO (Figure 4d). Besides, the positive-charged trimethylammonium group and large Van der Waal volume (361.5 Å^3) for

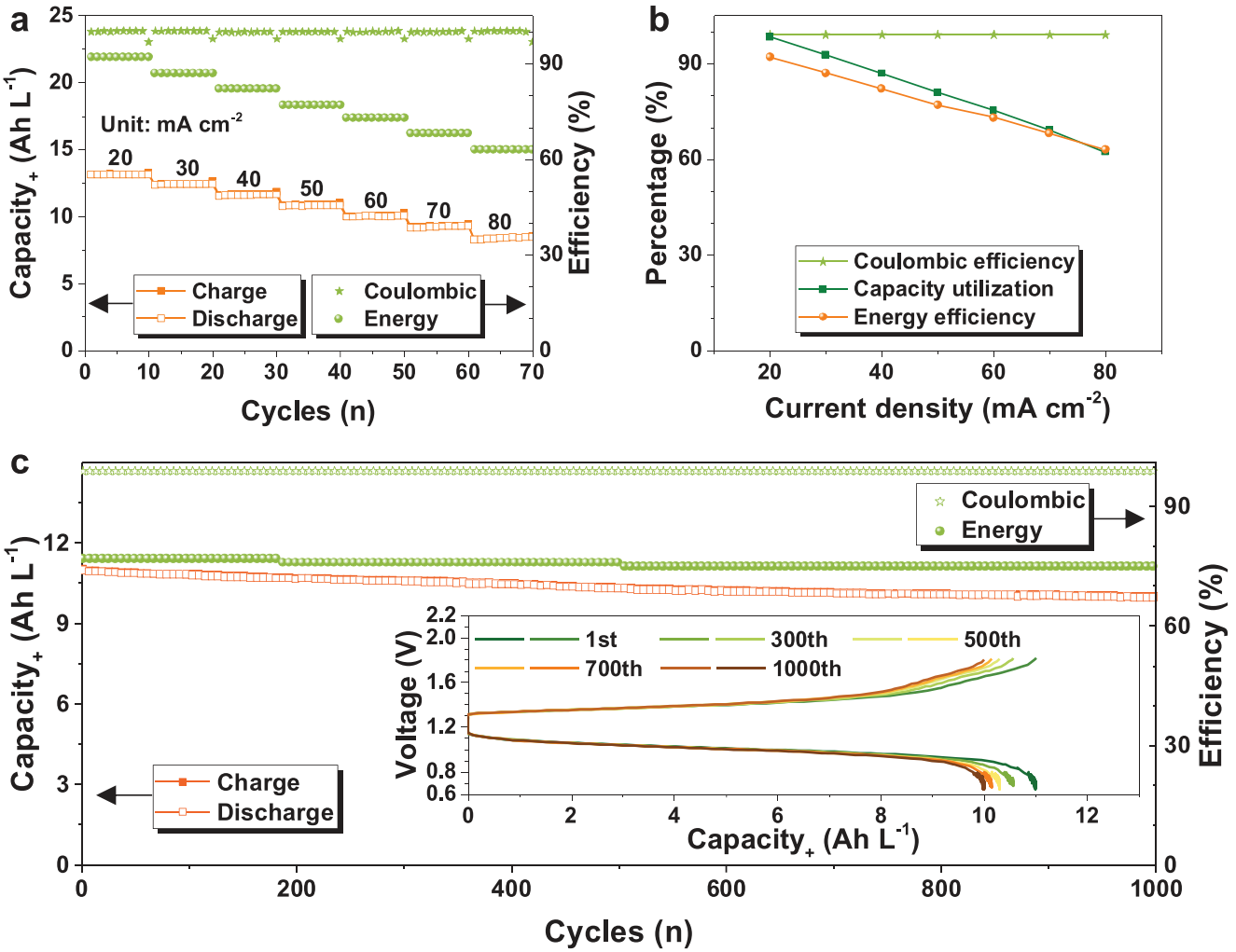

Figure 5. Performance of a concentrated TMAAcNH-TEMPO/$(NPr)_2V$ battery assembled with TMAAcNH-TEMPO (0.5 M) in catholyte (7.0 mL) and $(NPr)_2V$ (0.5 M) in anolyte (10.0 mL). a) Charge–discharge capacity, CE, and EE of the battery when galvanostatically cycled at a current density range of 20–80 mA cm^{-2}. b) The corresponding plots of CE, EE, and capacity utilization versus the current density of the battery. c) Galvanostatic cycling of the battery at 50 mA cm^{-2} for 1000 consecutive cycles. Charge–discharge capacity, EE, and CE are plotted as functions of the cycle number. The entire 1000 cycles occurred for ≈970 h. Inset in (c) is the charge–discharge curves of the battery at the 1st, 300th, 500th, 700th, and 1000th cycles, respectively.

TMAAcNH-TEMPO are beneficial to suppress the molecular crossover of an AEM. These combined effects synergistically result in the remarkable cycling stability of TMAAcNH-TEMPO.

Encouraged by the low fading rate of the 0.1 M TMAAcNH-TEMPO/$(NPr)_2V$ AORFB and high water-solubility (Figure 2c; Figure S21, Supporting Information), we then constructed a higher concentration TMAAcNH-TEMPO/$(NPr)_2V$ AORFB at 0.5 M (13.4 Ah L^{-1} and 16.4 Wh L^{-1}). The 0.5 M battery exhibits an excellent rate performance from 20 to 80 mA cm^{-2} with an increment of 10 mA cm^{-2} (**Figure 5**a). Approximately 100% CE is observed at all current densities during the consecutive galvanostatic cycles (Figure 5b). The capacity utilization and EE were recorded as 98% and 92% at 20 mA cm^{-2}, respectively, and gradually decreased at higher current densities due to the increased polarization (Figure S22, Supporting Information). Even at 80 mA cm^{-2}, the capacity utilization and EE are still maintained at 62% and 63% (Figure 5b). The battery was cycled continuously for 1000 cycles at 50 mA cm^{-2} over a period of 970 h or 40.4 days (Figure 5c; Figure S23, Supporting Information). The rather stable charge and discharge voltage profiles are observed at 1.38 and 1.02 V by average (Inset in Figure 5c). After 1000 cycles, the battery retains 86% of its original capacity, equivalent to an apparent capacity fade rate of 0.0144% h^{-1}. The capacity loss is primarily attributed to the slow crossover of TMAAcNH over extended cycling. The ^1H NMR spectrum of 0.5 M post-cycling catholyte shows no obvious change of decomposition into other species, as indicated by the lack of new signs in the aliphatic region (Figure S24, Supporting Information). This number is comparable to the 0.5 M TMAAcNH-TEMPO symmetric battery with a fade rate of roughly 0.0178%/h (Figure S25, Supporting Information). The 0.5 M TMAAcNH-TEMPO/$(NPr)_2V$ AORFB represents one of the most and stable and extensive cycled total organic flow batteries to date (Table S3, Supporting Information).

3. Conclusion

In summary, we have demonstrated a remarkably stable redox-active nitroxyl radical catholyte (TMAAcNH-TEMPO) with high solubility (4.30 M) for an all-organic AORFB. When paired with $(NPr)_2V$, the TMAAcNH-TEMPO/$(NPr)_2V$ AORFB displayed a long cycling life with a high capacity retention rate of ≈0.0144% h^{-1} over 40 days. We further clarified the stabilization mechanism of the TEMPO radical and found that the introduction of trimethylammonium and acetamido groups can effectively suppress the ring-opening side reaction and crossover. It is anticipated that the stability of TMAAcNH-TEMPO-based AORFB can be even further improved by the optimization of ion-exchange membranes. The presented battery and mechanistic studies open up new opportunities for developing TEMPO-based AORFBs toward massive-scale renewable energy storage.

Supporting Information

Supporting Information is available from the Wiley Online Library or from the author.

Acknowledgements

This study was financially supported by grants from the National Natural Science Foundation of China (Nos. 21875181), Natural Science Basic Research Program of Shaanxi (Program No. 2019JLP-13), Shaanxi Key Research and Development Project (No. 2019TSLGY07-05) and 111 Project 2.0 (BP2018008). T. Leo Liu and Wenda Wu thank National Science Foundation (Career Award, Grant No. 1847674) and Utah State University (faculty startup funds to Dr. T. Leo Liu) for supporting this study. Xiaohua Sun acknowledges the support by the 111 Project of the Ministry of Education of China (D20015).The authors would like to thank Ying Zhang, and Gang Chang at the Instrument Analysis Center of Xi'an Jiaotong University for the assistance of ESI-MS and NMR analyses. The authors would like to thank Lijing Ma at the State Key Laboratory of Multiphase Flow in Power Engineering of Xi'an Jiaotong University for the assistance of EPR measurements.

Conflict of Interest

The authors declare no conflict of interest.

Author Contributions

J.S. and T.L.L. supervised the project. J.S., H.F, and T.L.L. conceived and designed the experiments. H.F. conducted the experiments. R.M. synthesized the TEMPO molecules. W.W., H.L., and B.H. helped with the CV and RDE measurements and analysis. J.L. helped with the battery assembly and analysis. J.S., T.L.L., H.F., and W.W. discussed and analyzed the data. H.F., W.W., J.S., and T.L.L. wrote the manuscript. All authors reviewed and edited the manuscript.

Data Availability Statement

The data that support the findings of this study are available from the corresponding author upon reasonable request.

Keywords

energy storage, nitroxyl radicals, organic catholytes, redox flow batteries

Received: March 24, 2022
Revised: May 2, 2022
Published online:

[1] B. Obama, *Science* **2017**, *355*, 126.
[2] J. Luo, B. Hu, M. Hu, Y. Zhao, T. L. Liu, *ACS Energy Lett.* **2019**, *4*, 2220.
[3] P. Leung, A. A. Shah, L. Sanz, C. Flox, J. R. Morante, Q. Xu, M. R. Mohamed, C. Ponce de León, F. C. Walsh, *J. Power Sources* **2017**, *360*, 243.
[4] X. Wei, W. Pan, W. Duan, A. Hollas, Z. Yang, B. Li, Z. Nie, J. Liu, D. Reed, W. Wang, V. Sprenkle, *ACS Energy Lett.* **2017**, *2*, 2187.
[5] Y. Ding, Y. Zhao, Y. Li, J. B. Goodenough, G. Yu, *Energy Environ. Sci.* **2017**, *10*, 491.
[6] T. Liu, X. Wei, Z. Nie, V. Sprenkle, W. Wang, *Adv. Energy Mater.* **2016**, *6*, 1501449.
[7] C. DeBruler, B. Hu, J. Moss, J. Luo, T. L. Liu, *ACS Energy Lett.* **2018**, *3*, 663.
[8] J. Luo, B. Hu, C. Debruler, T. L. Liu, *Angew. Chem., Int. Ed.* **2018**, *57*, 231.
[9] J. Luo, B. Hu, C. Debruler, Y. Bi, Y. Zhao, B. Yuan, M. Hu, W. Wu, T. L. Liu, *Joule* **2019**, *3*, 149.
[10] S. Hu, T. Li, M. Huang, J. Huang, W. Li, L. Wang, Z. Chen, Z. Fu, X. Li, Z. Liang, *Adv. Mater.* **2021**, *33*, 2005839.
[11] B. Hu, C. DeBruler, Z. Rhodes, T. L. Liu, *J. Am. Chem. Soc.* **2017**, *139*, 1207.
[12] E. S. Beh, D. De Porcellinis, R. L. Gracia, K. T. Xia, R. G. Gordon, M. J. Aziz, *ACS Energy Lett.* **2017**, *2*, 639.
[13] G. Fang, J. Zhou, A. Pan, S. Liang, *ACS Energy Lett.* **2018**, *3*, 2480.
[14] T. Janoschka, N. Martin, M. D. Hager, U. S. Schubert, *Angew. Chem., Int. Ed.* **2016**, *55*, 14427.
[15] Y. Liu, M.-A. Goulet, L. Tong, Y. Liu, Y. Ji, L. Wu, R. G. Gordon, M. J. Aziz, Z. Yang, T. Xu, *Chem* **2019**, *5*, 1861.
[16] B. Hu, J. Luo, M. Hu, B. Yuan, T. L. Liu, *Angew. Chem., Int. Ed.* **2019**, *58*, 16629.
[17] M. R. Gerhardt, L. Tong, R. Gómez-Bombarelli, Q. Chen, M. P. Marshak, C. J. Galvin, A. Aspuru-Guzik, R. G. Gordon, M. J. Aziz, *Adv. Energy Mater.* **2017**, *7*, 1601488.
[18] Z. Yang, L. Tong, D. P. Tabor, E. S. Beh, M. - A. Goulet, D. De Porcellinis, A. Aspuru-Guzik, R. G. Gordon, M. J. Aziz, *Adv. Energy Mater.* **2018**, *8*, 1702056.
[19] K. Lin, R. Gómez-Bombarelli, E. S. Beh, L. Tong, Q. Chen, A. Valle, A. Aspuru-Guzik, M. J. Aziz, R. G. Gordon, *Nat. Energy* **2016**, *1*, 16102.
[20] A. Hollas, X. Wei, V. Murugesan, Z. Nie, B. Li, D. Reed, J. Liu, V. Sprenkle, W. Wang, *Nat. Energy* **2018**, *3*, 508.
[21] R. Feng, X. Zhang, V. Murugesan, A. Hollas, Y. Chen, Y. Shao, E. Walter, N. P. N. Wellala, L. Yan, K. M. Rosso, W. Wang, *Science* **2021**, *372*, 836.
[22] P. Leung, T. Martin, M. Liras, A. M. Berenguer, R. Marcilla, A. Shah, L. An, M. A. Anderson, J. Palma, *Appl. Energy* **2017**, *197*, 318.
[23] B. Yang, L. Hoober-Burkhardt, F. Wang, G. K. Surya Prakash, S. R. Narayanan, *J. Electrochem. Soc.* **2014**, *161*, A1371.
[24] Y. Xu, Y. Wen, J. Cheng, Y. Yanga, Z. Xie, G. Cao, *World Non-Grid-Connected Wind Power and Energy Conf. 2009. WNWEC 2009*, IEEE, Nanjing, China **2009**, pp 1–4.
[25] Y. Xu, Y.-H. Wen, J. Cheng, G.-P. Cao, Y.-S. Yang, *Electrochim. Acta* **2010**, *55*, 715.

[26] C. Zhang, Z. Niu, S. Peng, Y. Ding, L. Zhang, X. Guo, Y. Zhao, G. Yu, *Adv. Mater.* **2019**, *31*, 1901052.
[27] *ARPA-E GRIDS Program Overview*, http://arpa-e.energy.gov/sites/default/files/documents/files/GRIDS_ProgramOverview.pdf, Office of ARPR-E, Department of Energy, United States: **2011**.
[28] B. Hu, T. L. Liu, *Science* **2021**, *372*, 788.
[29] C. DeBruler, B. Hu, J. Moss, X. Liu, J. Luo, Y. Sun, T. L. Liu, *Chem* **2017**, *3*, 961.
[30] R. S. Nicholson, *Anal. Chem.* **1965**, *37*, 1351.
[31] H. Fan, J. Zhang, M. Ravivarma, H. Li, B. Hu, J. Lei, Y. Feng, S. Xiong, C. He, J. Gong, T. Gao, J. Song, *ACS Appl. Mater. Interfaces* **2020**, *12*, 43568.
[32] W. Zhou, W. Liu, M. Qin, Z. Chen, J. Xu, J. Cao, J. Li, *RSC Adv.* **2020**, *10*, 21839.
[33] B. Huskinson, M. P. Marshak, C. Suh, S. Er, M. R. Gerhardt, C. J. Galvin, X. Chen, A. Aspuru-Guzik, R. G. Gordon, M. J. Aziz, *Nature* **2014**, *505*, 195.
[34] C. X. Wang, Z. Yang, Y. R. Wang, P. Y. Zhao, W. Yan, G. Y. Zhu, L. B. Ma, B. Yu, L. Wang, G. G. Li, J. Liu, Z. Jin, *ACS Energy Lett.* **2018**, *3*, 2404.
[35] D. G. Kwabi, K. Lin, Y. Ji, E. F. Kerr, M.-A. Goulet, D. De Porcellinis, D. P. Tabor, D. A. Pollack, A. Aspuru-Guzik, R. G. Gordon, M. J. Aziz, *Joule* **2018**, *2*, 1894.
[36] A. Orita, M. G. Verde, M. Sakai, Y. S. Meng, *Nat. Commun.* **2016**, *7*, 13230.
[37] A. A. Shah, M. J. Watt-Smith, F. C. Walsh, *Electrochim. Acta* **2008**, *53*, 8087.
[38] T. Yamamura, N. Watanabe, T. Yano, Y. Shiokawa, *J. Electrochem. Soc.* **2005**, *152*, A830.
[39] M. Shibuya, F. Pichierri, M. Tomizawa, S. Nagasawa, I. Suzuki, Y. Iwabuchi, *Tetrahedron Lett.* **2012**, *53*, 2070.
[40] B. Wang, C. Rong, P. K. Chattaraj, S. Liu, *Theor. Chem. Acc.* **2019**, *138*, 124.
[41] Y. Li, Z. Xu, Y. Liu, S. Jin, E. M. Fell, B. Wang, R. G. Gordon, M. J. Aziz, Z. Yang, T. Xu, *ChemSusChem* **2021**, *14*, 745.